

ADVANCED GEOMETRY-BASED MODELING FOR MIMO SCENARIOS IN COMPARISON WITH REAL MEASUREMENTS

Giovanni Del Galdo¹, Jörg Lotze¹, Martin Haardt¹, and Christian Schneider²

Ilmenau University of Technology

1. Communications Research Laboratory
 2. Measurements Engineering Laboratory
- P.O. Box 100565
D-98684 Ilmenau, Germany

ABSTRACT

The scenario encountered in a recent measurement campaign undertaken at Ilmenau University of Technology has been artificially reconstructed in a computer-based propagation model for wireless communications developed by the authors. The real measurements have been collected with the RUSK MIMO multidimensional channel sounder (Thomä *et al.*, 2001). The program which implements the model includes a geometrical representation of the environment surrounding the experiment and a precise representation of the transmitting and receiving antennas. The analysis of all this information leads to a synthetic data set similar to the one actually measured. From the comparisons of the two channel matrices it is possible to derive useful information to improve the model itself and to better understand the physical origins of small-scale fading. In particular the effects of the different parameters on the synthetic channel have been studied in order to assess the sensibility of the model. This analysis shows that the correct positioning of a small number of scatterers is enough to achieve frequency selectiveness as well as specific traits of the channel statistics. The size of the scattering clusters, the number of scatterers per cluster, and the Rician K -factor can be modified in order to tune the channel statistics at will. To obtain higher levels of time variance, moving scatterers or time dependent reflection coefficients must be introduced.

1. INTRODUCTION

The high complexity of the propagation phenomenon sets a vast challenge in the effort of modeling the wireless channel. The most accurate approach would be to solve the Maxwell equations. However the computational effort required would be prohibitive, especially if we considered multiple antennas at both ends of the link, i.e., a MIMO system (Multiple Input Multiple Output). In fact, if M_R and M_T are the number of antennas at the receiver and at the

transmitter, respectively, the number of channels to be calculated grows to $M_R \cdot M_T$. Furthermore a precise physical and geometrical description of the objects would be necessary.

In order to reduce the complexity of the model the so called GTD (Geometric Theory of Diffraction) can be employed (Correia, 2001). This approach postulates the existence of direct, diffracted and reflected rays only. As the wavelength λ approaches zero, this approximation becomes increasingly accurate.

With a ray-tracing engine and a full 3D description of the environment it is then possible to calculate all possible rays linking the antennas. However with a GTD approach a complete geometrical representation of the scenario is still required. A further approximation is to simplify the geometry surrounding the antennas with a discrete number of reflectors, called *scatterers*; when only direct and reflected rays are considered the computational complexity drops significantly. In this paper we present a simplified model which generates channels which mimic most characteristics of typical outdoor real measured channels. To this aim it is extremely important to determine which features of the synthetic channel are affected by the different parameters present in the model. A relatively low computational complexity allows us to generate channels with all possible combinations of values for the parameters. Then we analyze the data by finding strong traits which link a particular parameter to a particular feature. At the same time we are able to assess whether a parameter has no effect on a specific feature.

This extensive search and its results are reported in section 3. Then we modeled the scenario found in one of the measurement campaigns undertaken at Ilmenau University of Technology. Section 4 reports the direct comparison between the synthetic and real channels which led to a better understanding on the origins of the fast and slow fading processes. The knowledge derived in section 3 was tested on

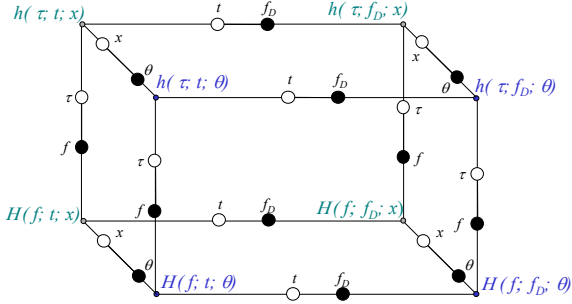


Fig. 1. The four Bello functions extended to the spatial domain, in time t , frequency f , delay time τ , Doppler frequency f_D , angle θ , aperture x , and their Fourier transform relationships.

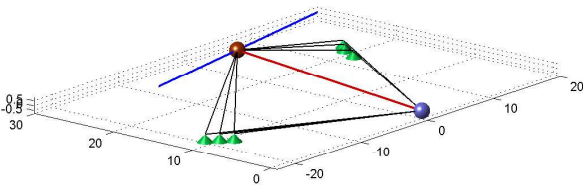


Fig. 2. In this simple model 6 scatterers (cones) link the receiver and the transmitter. The path of the transmitter and the LOS path are also visible.

this scenario. Lastly, section 5 draws the conclusions.

2. A GEOMETRY-BASED CHANNEL MODEL

The geometry-based channel model developed at TU Ilmenau relies entirely on GTD and has been designed to simulate a fully 3D Multi-User-MIMO scenario. It has been simplified to single-bounce reflections in order to reduce the computational complexity. Clusters of scatterers can be arbitrarily positioned in the 3D reconstruction of the environment. Each scatterer corresponds to a single ray and is characterized by a complex coefficient which, for simplicity, is independent of the Direction of Arrival and the Direction of Departure (DoA and DoD); but may vary in time with an arbitrary law. The coefficient determines the phase shift and power attenuation introduced by the scatterer.

The receiver thus receives a number of rays equal to the number of scatterers plus the Line Of Sight LOS, which links the transmitter to the receiver directly. Figure 2 shows a simple example of this modeling approach. Such a simplified model still requires a fairly high computational complexity because the total number of rays to be computed is: $M_R \cdot M_T \cdot N_{scat}$.

The advantage of a geometry-based model with respect

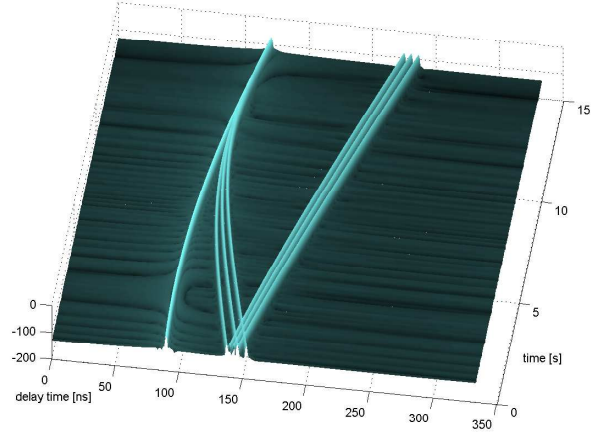


Fig. 3. This plot shows the Channel Impulse Responses of the model seen in Fig. 2. The arrival times move as the transmitter moves on its path.

to a stochastic one is indeed the possibility to easily generate a frequency selective time variant channel. In fact the frequency selectiveness is caused by the multi-path effect while the time variance is set off by the movement of the antennas and of the scatterers as well as the varying scattering coefficients with respect to time. In other words it well models a typical frequency selective time variant radio channel. In order to describe completely such a channel we need to describe it in one of the four possible two-dimensional domains named the Bello domains. (Bello, 1963). Either $\{t, f\}$, $\{t, \tau\}$, $\{f_D, f\}$ or $\{f_D, \tau\}$ where t , f_D , f , and τ denote time, Doppler frequency, frequency, and delay time, respectively. The most convenient domain in which to compute the channel is certainly $\{t, f\}$. Having a geometrical representation of all objects in time makes the choice of t over f_D quite obvious. The choice of f over τ requires more explanation. Thanks to the geometrical representation it is simple to calculate the path lengths for each ray present in the scenario. Assuming that the velocity of light, c , is equal to the velocity of all rays, we can calculate the delay time associated with every ray, i.e., the time needed to reach the receiver. The delay times found will not necessarily match the sampling grid chosen. For this reason more processing is required. On the contrary, in the frequency domain we can calculate the channel response for the specific frequency bins that we are interested in. The choice of a specific Bello domain is at the end a matter of convenience since it is possible to derive the other representations via Fourier transforms as displayed in figure 1. For instance, having $H(f, t)$, i.e., the channel expressed in delay time and time, we can calculate $h(\tau, t)$, the channel in frequency and time, as:

$$h(\tau, t) = \int H(f, t) e^{j2\pi f \tau} df. \quad (1)$$

Figure 3 shows the channel impulse response in delay time τ and time t . The channel was originally computed in the

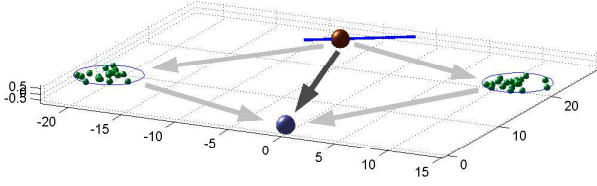


Fig. 4. The geometrical representation of the model \mathcal{M}_α . Two scattering clusters and a strong LOS are visible. The transmitter (at the top) moves on a linear path.

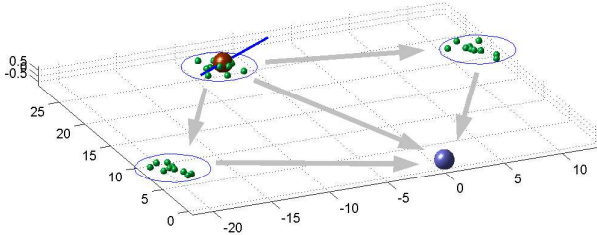


Fig. 5. The geometrical representation of the model \mathcal{M}_β . The model is characterized by three scattering clusters; one of them surrounds the transmitter.

$\{t, f\}$ domain from the geometry displayed in figure 2. Via a proper Fourier transform the CIR in $\{t, \tau\}$ can be conveniently calculated.

The amplitude and phase of each ray are calculated separately at the receiver. The phase of the i -th ray at a certain time snapshot t_o and frequency f_o are calculated as follows:

$$\varphi_i(t_o, f_o) = \angle(e^{-j2\pi\frac{f_o}{c}L_i}) + \theta_i, \quad (2)$$

where L_i is the ray's path-length and θ_i is the phase shift introduced by the scatterer. The amplitude depends simply on the scattering coefficient, antenna gain, and path-loss.

3. AN EXHAUSTIVE INVESTIGATION

The first step in understanding how sensible the model is to the different parameters and which features of the synthetic channel are affected, is to model some typical scenarios and to generate channels with all possible values for the parameters. We implemented two models, to which we will refer as \mathcal{M}_α and \mathcal{M}_β , seen in figures 4 and 5. \mathcal{M}_α models a typical scenario in which the areas around the transmitter and the receiver are free of scatterers while some are present in the middle of the link. \mathcal{M}_β , on the other hand, models a scattering cluster in the proximity of the transmitter. We generated each channel for the following sampling grid:

- A bandwidth B of 400 MHz at a center frequency of 1 GHz sampled with a $\Delta f = 1.3$ MHz for a total of 301 samples.

- A total of 200 time snapshots were taken, one every 10 ms for a total of 2 seconds.

The choices of these parameters determine the sampling grids in the coupled domains. In fact if the complex base-band signal is sampled in the range $[-\frac{B}{2}, \frac{B}{2}]$, then $\Delta\tau$, the resolution in delay time, is equal to $\frac{1}{B}$. In the same way the bandwidth in the Doppler frequency, $2 \cdot f_{D,max}$ can be calculated from the resolution in time Δt as:

$$f_{D,max} = \frac{1}{2 \cdot \Delta t}. \quad (3)$$

- The resolution in delay time is $\Delta\tau = 2.5$ ns, which corresponds to a distance of less than a meter (75 cm). We can successfully resolve (i.e., without aliasing) up to paths 220 meters long.
- Doppler shifts up to $f_{D,max} = \pm 50$ Hz are visible without aliasing.

The transmitter moves with a uniform velocity of about 5 m/s. Both transmitter and receiver employ a ULA (Uniform Linear Array) with $M_R = M_T = 4$ antennas spaced by $\frac{\lambda}{2}$.

After several experiments with different geometries and different configurations we narrowed down our extensive search to three dominant parameters:

- Cluster size
- Number of scatterers per cluster
- Rician K -factor

A fourth dominant parameter is certainly the modeling of the reflection coefficients, and more importantly their trend in time. This leaves, however, too many degrees of freedom since we could implement any arbitrary function to describe it in time. For this reason we left this important parameter to future and more specific investigations. In our simulations the reflection coefficients are kept constant along all dimensions, i.e., frequency and time. The Rician K -factor is defined as

$$K = \frac{P_{LOS}}{P_{scatt}}, \quad (4)$$

i.e., the power attributed to the Line Of Sight divided by the power of the scatterers. Clearly it is a function of the path-losses which on their side are determined by the geometry, the transmit power, and the reflection coefficients. We scale the amplitudes of the reflection coefficients to obtain a desired K -factor.

We then generate many channels with different values for these three parameters and then analyze the data to find any strong dependency.

3.1. K -factor

The K -factor affects different features of the channel. Firstly it influences its variance with respect to all four domains. It

is thus very interesting to assess this information quantitatively computing the RMS delay spread τ_{RMS} , the coherence bandwidth $(\Delta f)_c$, the RMS Doppler spread $f_{\text{D,RMS}}$ and the coherence time $(\Delta t)_c$.

The RMS delay spread of the channel, τ_{RMS} , is derived from the multipath intensity profile $\psi_{De}(\tau)$ which represents the average power of the channel output as a function of delay time ((A. Paulraj and Gore, 2003), (Stüber, 1996)).

$$\tau_{\text{RMS}} = \sqrt{\frac{\int_0^{\tau_{\text{max}}} (\tau - \bar{\tau})^2 \psi_{De}(\tau) d\tau}{\int_0^{\tau_{\text{max}}} \psi_{De}(\tau) d\tau}}. \quad (5)$$

τ_{max} is the maximum delay spread while $\bar{\tau}$ is the average delay spread given by

$$\bar{\tau} = \frac{\int_0^{\tau_{\text{max}}} \tau \psi_{De}(\tau) d\tau}{\int_0^{\tau_{\text{max}}} \psi_{De}(\tau) d\tau}. \quad (6)$$

The coherence bandwidth $(\Delta f)_c$ corresponds to the frequency lag in which the channel's autocorrelation function reduces to 0.7. As previously described, the channel representations in the four domains are coupled through Fourier transforms. For this reasons $(\Delta f)_c$ and τ_{RMS} are connected as well. In fact the coherence bandwidth is inversely proportional to the RMS delay spread so that

$$(\Delta f)_c = \frac{\text{const}_1}{\tau_{\text{RMS}}}. \quad (7)$$

The same concepts are applied on the $\{f_D, t\}$ pair. The RMS Doppler spread, $f_{\text{D,RMS}}$, is derived in a similar way from ψ_{Do} , the Doppler power spectrum, which corresponds to the average power as a function of Doppler frequency f_D .

$$f_{\text{D,RMS}} = \sqrt{\frac{\int_{\mathcal{F}} (f_D - \bar{f}_D)^2 \psi_{Do}(f_D) \bar{f}_D}{\int_{\mathcal{F}} \psi_{Do}(f_D) \bar{f}_D}}$$

$$\bar{f}_D = \frac{\int_{\mathcal{F}} f_D \psi_{Do}(f_D) \bar{f}_D}{\int_{\mathcal{F}} \psi_{Do}(f_D) \bar{f}_D}$$

The integration domain, \mathcal{F} , corresponds to the Doppler frequency interval where the Doppler power spectrum is non zero. The coherence time $(\Delta t)_c$ is calculated in the same way as the coherence bandwidth. It corresponds to the time lag at which the autocorrelation function drops to 0.7. $(\Delta t)_c$ indicates how time variant the channel is and similarly to the $\{f, \tau\}$ pair

$$(\Delta t)_c = \frac{\text{const}_2}{f_{\text{D,RMS}}} \quad (8)$$

Figure 6 shows typical trends for τ_{RMS} , $f_{\text{D,RMS}}$, $(\Delta f)_c$, and $(\Delta t)_c$ for different K -factors. Similar plots can be observed for both models \mathcal{M}_α and \mathcal{M}_β for almost any cluster size and number of scatterers. As K grows τ_{RMS} decreases, meaning that the channel becomes rapidly less frequency selective. The same observation can be derived from the trend of $(\Delta f)_c$. $f_{\text{D,RMS}}$ and $(\Delta t)_c$ show the same trends. For bigger K 's the channel becomes increasingly less time variant. The two constants const_1 and const_2 are plotted

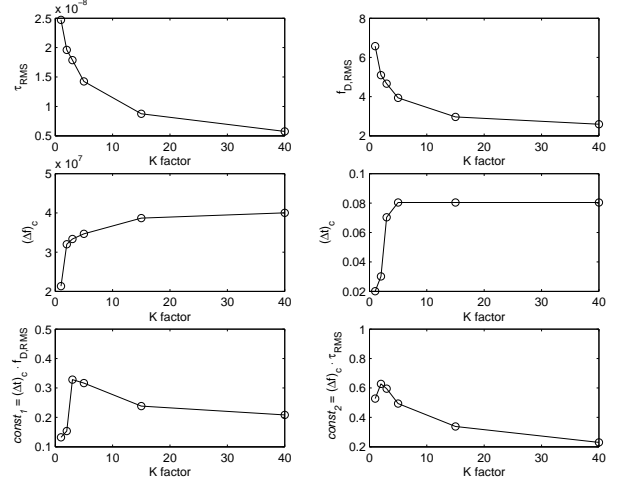


Fig. 6. τ_{RMS} , $f_{\text{D,RMS}}$, $(\Delta f)_c$ and $(\Delta t)_c$ plotted for different K -factors.

as well to show that the inverse proportionality expressed in equations (7) and (8) holds.

Another interesting measure of the variation of the channel is to look at the fluctuation of $\|\mathbf{H}\|_F^2$. A good index is the so called *coefficient of variation* (Nabar, 2003) which is commonly used as a quantitative measure of the spread (fluctuation) of a random variable. The coefficient of variation ξ is defined as:

$$\xi = \frac{\sqrt{E\{(\|\mathbf{H}\|_F^2)^2\} - (E\{\|\mathbf{H}\|_F^2\})^2}}{E\{\|\mathbf{H}\|_F^2\}}. \quad (9)$$

We calculated ξ for all frequency bins to discover that for growing K 's the coefficient of variation becomes increasingly smaller (Figure 7). This is actually expected if we associate ξ with the *effective diversity order*, as described in (Nabar, 2003).

In fact the effective diversity order, N_{div} , can be written as:

$$N_{\text{div}} = \frac{1}{\xi^2}, \quad (10)$$

and it approaches infinity for a channel with only the LOS component (AWGN channel) while $N_{\text{div}} = M_R \cdot M_T$ for Rayleigh channels. The trend in ξ and consequently in N_{div} can be observed for both models proposed and independently from other parameters.

Another interesting analysis can be performed on the statistics of the eigenvalues. Figure 8 shows their distributions for different K -factors for the model \mathcal{M}_α . Eigenvalue decompositions have been applied on the spatial correlation matrices at the receiver \mathbf{R}_R calculated for each time snapshot. Then we generated the histograms to derive the amplitudes distribution on a dB scale. The spatial correlation matrix \mathbf{R}_R at the receiver for the specific time t_o is:

$$\mathbf{R}_R(t_o) = \frac{1}{F} \sum_{i=1}^F \mathbf{H}(:, :, i, t_o) \cdot \mathbf{H}(:, :, i, t_o)^H, \quad (11)$$

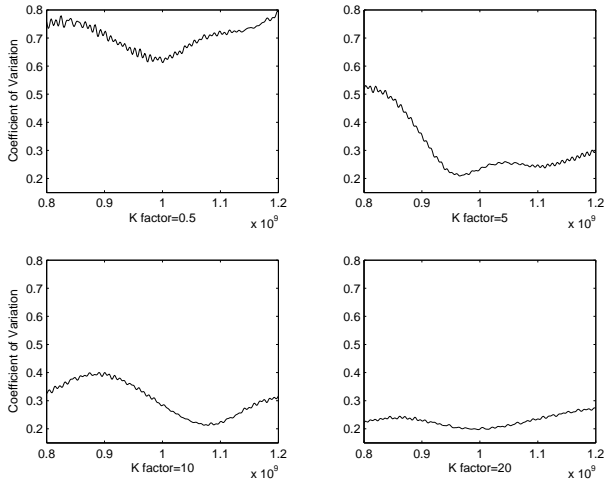


Fig. 7. The *coefficient of variation* ξ plotted against frequency f for different K -factors.

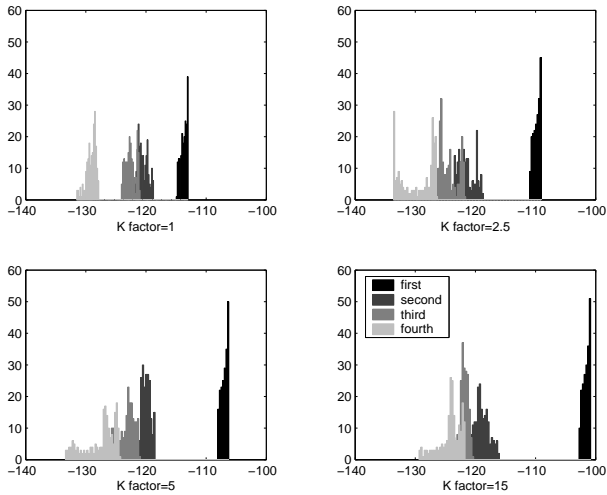


Fig. 8. Eigenvalue distributions in dB as K grows for \mathcal{M}_α .

where F is the total number of frequency bins, \mathbf{H}^H is the Hermitian transpose of \mathbf{H} and the channel \mathbf{H} has dimensions $M_R \times M_T \times F \times T$. The MATLAB like notation $\mathbf{H}(:, :, i, t_o)$ denotes the bidimensional channel matrix $\mathbf{H} \in \mathbb{C}^{M_R \times M_T}$ for a specific frequency $f = i$ and time $t = t_o$. Figure 8 shows the distributions of the eigenvalues plotted in dB. The channels have been generated without noise and without any normalization, i.e., the absolute amplitudes of the eigenvalues appear very low (around -120 dB). This has no physical meaning and only the relative distances between the eigenvalues should be taken into account. As the K -factor grows, the Line Of Sight becomes increasingly stronger and the channel displays low rank traits. In other words the strongest eigenvalue separates itself from the weaker ones as K increases.

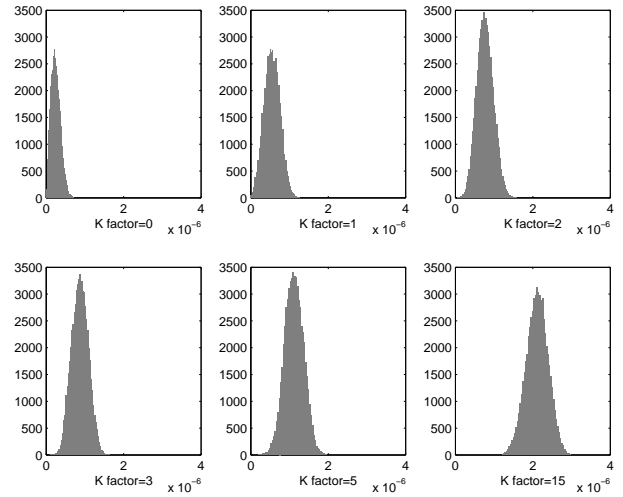


Fig. 9. Amplitude distributions of channels considering all frequencies and time snapshots for different Rician K -factors for \mathcal{M}_α .

A higher K -factor inhibits the effects of the fast-fading. This can be easily seen by plotting the distributions of the amplitudes of the channel considering all frequencies and time snapshots (figure 9).

3.2. Cluster Size and Number of Scatterers

The analysis on different cluster sizes and number of scatterers led to more unexpected results. While the relationship of the Rician K -factor with the different channel statistics can be easily explained, the effects induced by the cluster size and number of scatterers are not so obvious. In the first simulations we investigated whether the geometrical distribution affected the channel. We generated clusters with scatterers distributed uniformly on a sphere, on a circle on the horizontal plane (as seen in figures 4 and 5) and on the surface of a cylinder or a sphere. All channels showed the same trends and for this reason we continued with more detailed investigations fixing the distribution of the scatterers on a circle. We generated models with cluster sizes with diameters ranging from $\frac{\lambda}{2}$ to 20λ and with numbers of scatterers ranging from 1 up to 100 reflection points per cluster.

We then investigated trends in the different channel features fixing all parameters as either the cluster size or the number of scatterers changed. All features but the effective diversity order did not show any strong dependency even though they were all affected. For instance, increasing the size of the scattering clusters affects the frequency selectiveness of the channel, even though there is neither a direct nor an inverse proportionality between the two. Figure 10 shows the effective diversity order N_{div} plotted for different frequencies f and for different cluster diameters expressed

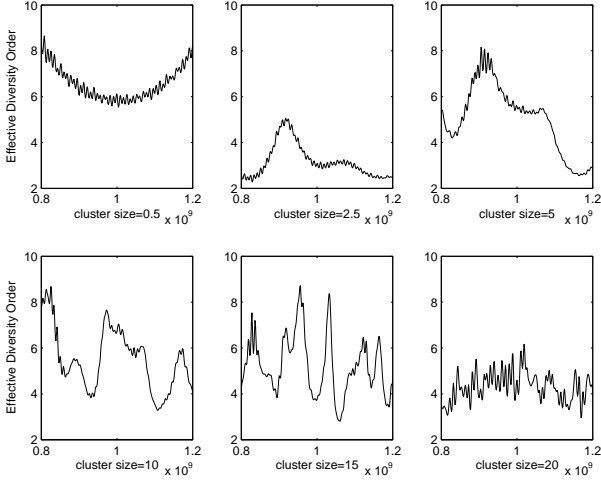


Fig. 10. The *effective diversity order* N_{div} plotted against frequency f for different cluster sizes (expressed in λ 's) for \mathcal{M}_β .

in λ 's for the first model, \mathcal{M}_α . Analyzing N_{div} along different frequencies we can recognize a slow-moving trend corrupted by faster variations. For instance, in the first plot of figure 10 (cluster size = 0.5λ), we see a slow moving trend which looks like a concave semicircle summed by a zero mean noise-like process which introduces fast variations. After many simulations we observed that the magnitude of the fast moving N_{div} changed at every realization while the variance of the slow moving N_{div} changed with the cluster diameter with an undoubtedly direct proportionality. In other words, for bigger cluster sizes, N_{div} changes more rapidly along frequency while this does not necessarily correspond to higher frequency selectiveness nor to greater time variance. The number of scatterers affects the channel in a similar way but with a much weaker dependency.

4. A COMPARISON WITH REAL MEASUREMENTS

In order to assess the results derived in section 3 with an even more realistic scenario we modeled the surroundings of a measurement campaign undertaken at TU Ilmenau. Additionally the simulation allowed us to investigate the importance of other critical parameters of the model: the positions of the scatterers and the modeling of the reflection coefficients. The first step was to determine whether a rough positioning of the scatterers was enough to recreate the main features which characterize the measured channel. To this end, we chose, among the many measurements gathered, a channel with a strong LOS and characterized by a simple geometry so that the position of the scatterers could eas-

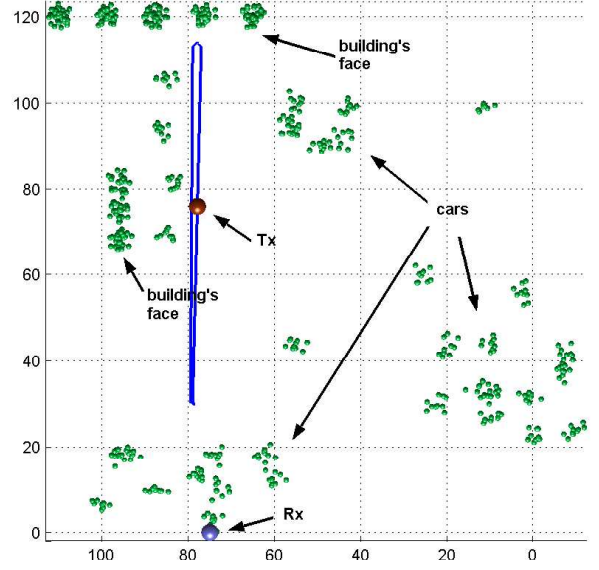


Fig. 11. Bird's eye view of the synthetic reconstruction of the scenario where the real measurements were taken.

ily be estimated. Figure 11 shows the bird's eye view of the reconstructed scenario. The receiver was a 4×8 polarization sensitive patch-array URA (Uniform Rectangular Antenna) and it was positioned by a window on the second floor of a building. The transmitter was a single 2 GHz omnidirectional antenna mounted on a wheeled cart pulled by hand up a road in the direction of a second building (figure 14). The transmitter path is represented by a continuous line in figure 11. In the proximity of the building the cart was turned around and pulled in the opposite direction (towards the receiver) approximately on the same path. The whole measurement took approximately 1 minute at a speed of 3 meters per second. The measurement device employed was the broadband real-time channel sounder RUSK MIMO from MEDAV (Molisch, 2002). The following parameters characterize the measurements:

- A bandwidth B of 120 MHz at a center frequency of 1.95 GHz sampled with $\Delta f = 300$ kHz for a total of 385 samples.
- A total of 6313 time snapshots were taken, one every 9.2 ms for a total of 58 seconds.

The same parameters were chosen for the synthetic model so that the two data sets had same dimensions and sampling grids. However, in order to compare the real measurements with the synthetic channels, adding the noise and performing a proper normalization must be taken into account.

The need for a normalization is due to the fact that the absolute powers sent by the antennas have not been considered. Only the relative difference in power between the LOS

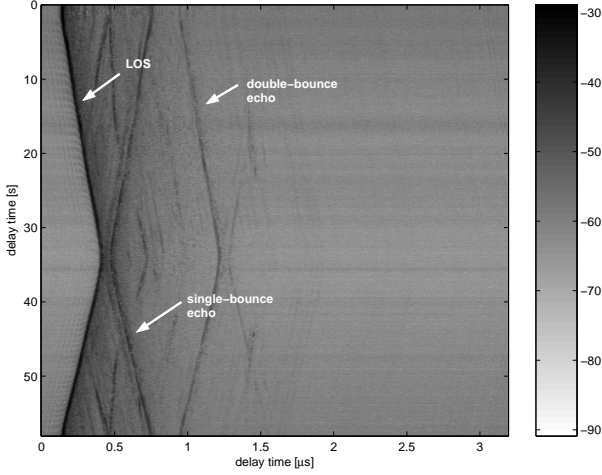


Fig. 12. Channel Impulse Responses from the real measurements in time t and delay time τ . The Line Of Sight LOS and echos are clearly visible. The grayscale represents amplitudes in a dB scale

and the scattering components have been modeled through the Rician K -factor which can be set at will. This simplified the modeling effort even though the results need post-processing in order to be finally compared with real measurements. The normalization is performed in such a way that the total power received for the synthetic channel matches the one received in the measurements. Clearly both data sets must have the same number of samples, dimensions and more in general, the same sampling grids. If \mathbf{H}_R denotes the channel for the real measurements and \mathbf{H}_M the synthetic one then the whole channel matrix must be scaled so that

$$\sum_{\Theta} |\mathbf{H}_R|^2 = \sum_{\Theta} |\mathbf{H}_M|^2 \quad (12)$$

where Θ spans the complete domain of all dimensions. In our simulations \mathbf{H}_M has been generated without noise. The normalization and the adding of the noise must then be done concurrently. First we have to estimate the power of the noise from the measurements. We assume constant AWGN (Additive White Gaussian Noise) over all dimensions (delay time, time, antennas, etc.). An effective way to measure the noise floor in the measurements is to observe the channel matrix in the time and delay time domain. If the path lengths are short enough, so that the last echoes extinguish before the maximum delay resolvable, we have a measurement of the noise without signal. If the number of samples is sufficient we can use this data to estimate the power of the noise. The noisy synthetic channel will then be

$$\mathbf{H}_{M, \text{noisy}} = \mathbf{H}_{M, \text{noiseless}} + \mathbf{H}_w, \quad (13)$$

where \mathbf{H}_w is a matrix whose elements are ZMCSCG (Zero Mean Circular Symmetric Complex Gaussians) random numbers with variance σ^2 .

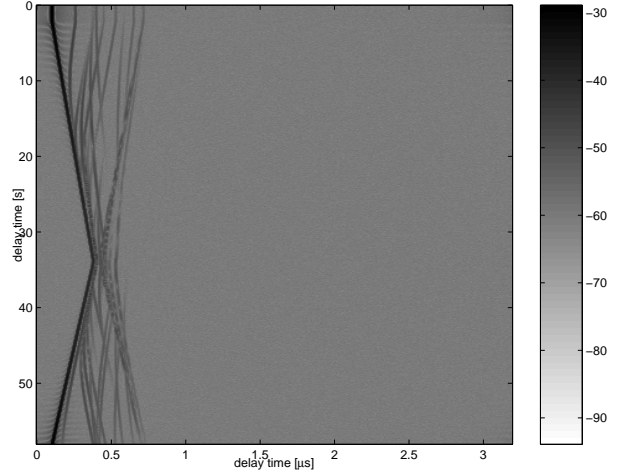


Fig. 13. The synthetically generated Channel Impulse Responses in time t and delay time τ .

Equation (12) then becomes:

$$\sum_{\Theta} |\mathbf{H}_R|^2 - \gamma \cdot \sigma^2 = \sum_{\Theta} |\mathbf{H}_M|^2, \quad (14)$$

where γ is the total number of samples present in \mathbf{H} , i.e., $\gamma = M_R \times M_T \times T \times F$, where T and F are the number of time snapshots and frequency bins respectively.

The geometry has been roughly reconstructed with the help of blueprints of the area and through visual inspection. Cars, buildings, light poles, and trash bins have been identified as the probable sources of scattering. Figure 12 shows the channel impulse responses in time t and delay time τ . The channel has been gathered originally in the $\{t, f\}$ domain; the CIRs in delay time have been computed via the Fourier transform described in equation (1). The LOS is clearly visible and as expected its delay lag grows as the transmitter moves farther away from the receiver. When the cart is turned around and pulled back towards the receiver, the arrival delay time decreases. Many echoes are visible as well. Note that as the transmitter moves most echoes arrive earlier, meaning that their path length becomes smaller. When the curve corresponding to one echo changes in time with the same slope characterizing the Line Of Sight, then we can deduce that the path length of the echo changes with the same rate of the path length of the LOS. The strong echo labeled *double-bounce echo* has the same trend as the LOS just delayed by approximately $0.8 \mu\text{s}$, which corresponds to 240 m, the distance between the top and bottom buildings doubled. For this reason it is very likely that this arrival corresponds to the signal reflected by the bottom building first, and then by the top building, thus a double-bounce echo. Figure 13 shows the channel generated by our model. The trend of the LOS is extremely well reproduced. This was, however, expected since the LOS is



Fig. 14. The receiver (top circle) and the transmitting antenna (bottom circle) mounted on a cart.

the only component easily predictable once the position of the transmitter is known. Most of the scattering contributions can be observed in the synthetic data set as well, with the exception of the double-bounce paths which have been omitted. Analyzing the two data sets in the $\{t, \tau\}$ domain suggests improvements in the modeling approach: in the real measurements we can observe that certain echo traces are stronger than others. In the modeled channel this does not happen. This is a result of the modeling of the reflection coefficients. In fact while their phase has been generated uniformly distributed in the $[0, 2\pi]$ range, the amplitude has been taken equal for all. The comparison suggests that the reflection coefficients need a more sophisticated description. Furthermore, a closer look on the real measurements reveals that some echoes exist only in certain time periods. This suggests that the amplitude of the reflection coefficients (perhaps their phases too) should be dependent on the Direction of Arrival and Direction of Departure (DoA and DoD). Figure 15 shows the fluctuations of the amplitudes of the channel for a specific frequency f_o plotted against time for the first 25 seconds. Fast-fading characterizes both signals even though the real measurements appear somehow more variant. In order to assess this feature quantitatively we compute the multipath intensity profile $\psi_{De}(\tau)$, the Doppler power spectrum $\psi_{Do}(f_D)$ and the autocorrelation functions in frequency $acf(\Delta f)$ and time $acf(\Delta t)$ for both data sets. From their analysis we can obtain the RMS delay spread τ_{RMS} , the coherence bandwidth $(\Delta f)_c$, the RMS Doppler spread $f_{D,RMS}$ and the coherence time $(\Delta t)_c$ (figures 16 and 17). The RMS delay spread shows that the energy is similarly distributed in delay time τ . In the real measurements two more spikes can be observed. This is due to the fact that two specific echoes have a significantly stronger magnitude compared to other echoes. The RMS delay spread τ_{RMS} is anyhow very similar suggesting

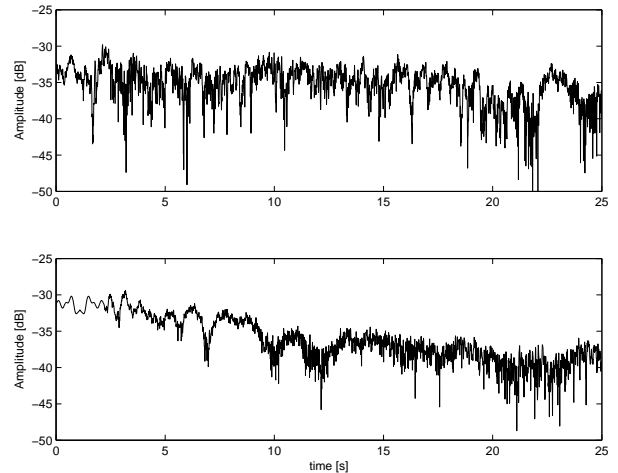


Fig. 15. Amplitudes of the CIRs for a specific frequency bin plotted in dB against time for the real measurements (top) and the model (bottom).

that the two channels will have a similar frequency selectiveness. The RMS delay spread corresponds to the distance between the two vertical lines plotted in figures 16 and 17. From the autocorrelation function in the frequency domain $acf(\Delta f)$ we can derive the coherence bandwidth $(\Delta f)_c$ which confirms that the two channels have approximately the same coherence bandwidth. In the $\{t, f_D\}$ pair the two channels show more differences. While the Doppler power spectrum $\psi_{Do}(f_D)$ has very similar trends, the autocorrelation function in the time domain shows that the measured channel is much more time variant than the synthetic one. Furthermore this analysis proves that equation (8) only represents a good empirical law, valid in most but not all cases. In figure 15 we can in fact recognize that the real measurements have a faster moving small-fading effect, especially during the first 10 seconds. We then investigated how we could generate more time variance changing only positions, the size of the scattering clusters, and the number of scatterers per cluster, and discovering that this was not possible. Our simulations showed that in order to achieve higher order of time variance it is absolutely necessary to model time variant reflection coefficients or to introduce moving scatterers along the time dimension.

5. CONCLUSIONS

Our simulations show that for certain modeling applications a simple GTD single-bounce model can mimic most channel features with sufficient precision, among which the frequency selectiveness and the time variance are the most characterizing. A rough positioning of the scattering clusters allows us to achieve a desired frequency selectiveness as well as other specific traits of the channel statistics by

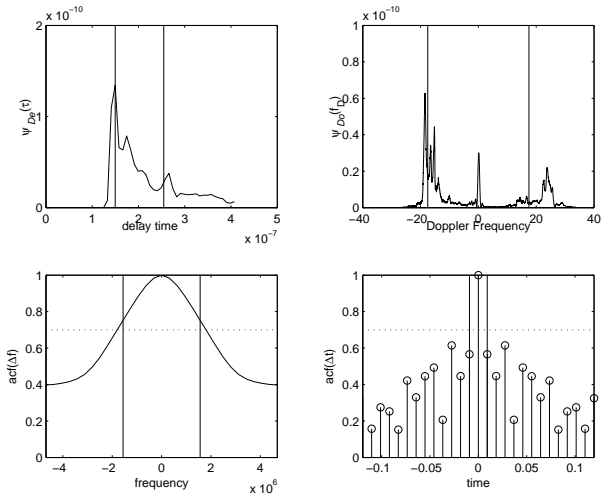


Fig. 16. The multipath intensity profile $\psi_{De}(\tau)$, Doppler power spectrum $\psi_{Do}(f_D)$ and the autocorrelation functions in frequency $acf(\Delta f)$ and time $acf(\Delta t)$ for the real measurements

tuning three basic parameters, i.e, the size of the scattering clusters, the number of scattering coefficients, and the Rician K -factor. To obtain higher levels of time variance and more realistic synthetic channels, moving scatterers and time dependent reflection coefficients must be modeled as well.

Acknowledgments

The authors gratefully acknowledge the support of MEDAV (www.channelsounder.de) in performing the channel measurements.

6. REFERENCES

- A. Paulraj, R. Nabar and D. Gore (2003). *Introduction to space-time wireless communications*. Cambridge University Press. Cambridge.
- Bello, P. (1963). Characterization of randomly time-variant linear channels. *IEEE Trans. Comm. Syst.* **11**, 360–393.
- Correia, Luis M. (2001). *Wireless Flexible Personalised Communications*. Wiley.
- Molisch, A.F.; Steinbauer, M.; Toeltsch M.; Bonek E.; Thomä R.S. (2002). Capacity of MIMO systems based on measured wireless channels. *IEEE Journal on Selected Areas in Communications* **20**(3), 561–569.
- Nabar, Rohit U. (2003). *Performance Analysis and Transmit*

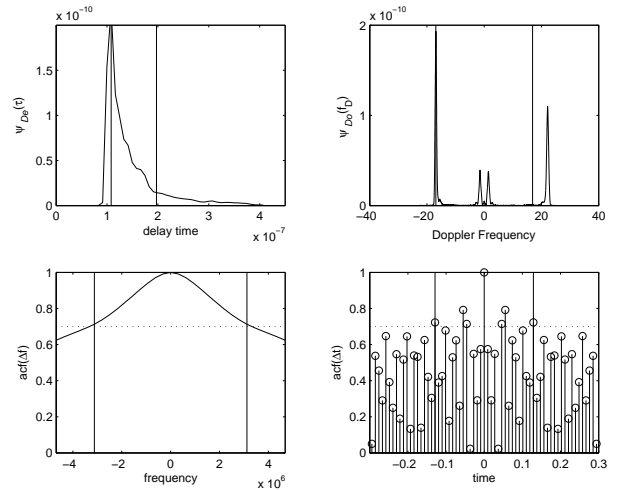


Fig. 17. The multipath intensity profile $\psi_{De}(\tau)$, Doppler power spectrum $\psi_{Do}(f_D)$ and the autocorrelation functions in frequency $acf(\Delta f)$ and time $acf(\Delta t)$ for the model

Optimization for General MIMO Channels. Doctoral Dissertation. Stanford.

Stüber, G. (1996). *Principles of Mobile Communication*. Kluwer. Norwell, MA.

Thomä, R.S., D. Hampicke, A. Richter, G. Sommerkorn and U. Trautwein (2001). MIMO vector channel sounder measurement for smart antenna system evaluation. *European Transaction on Telecommunications, Special issue on smart antennas*.